

# Characterization of PDMS Microchannels Using Horizontally or Vertically Formed 3D-Printed Molds by Digital Light Projection

Dong Hyun Han,<sup>‡</sup> Untaek Oh,<sup>‡</sup> and Je-Kyun Park\*Cite This: *ACS Omega* 2023, 8, 19128–19136

Read Online

ACCESS |



Metrics &amp; More

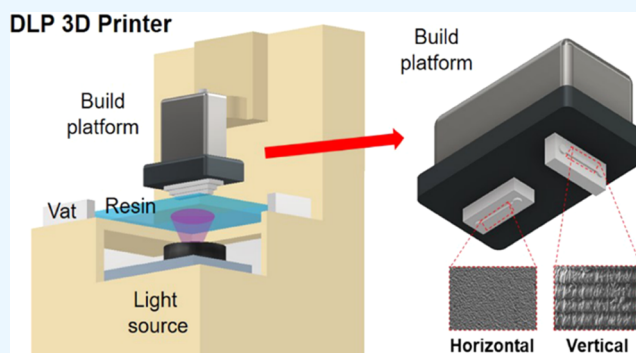


Article Recommendations



Supporting Information

**ABSTRACT:** Three-dimensional (3D) printing is one of the promising technologies for the fabrication of microstructures due to its versatility, ease of fabrication, and low cost. However, the direct use of 3D-printed microstructure as a microchannel is still limited due to its surface property, biocompatibility, and transmittance. As an alternative, rapid prototyping of poly-(dimethylsiloxane) (PDMS) from 3D-printed microstructures ensures both biocompatibility and efficient fabrication. We employed 3D-printed molds fabricated using horizontal and vertical arrangement methods with different slice thicknesses in a digital light projection (DLP)-based 3D printing process to replicate PDMS microchannels. The replicated PDMS structures were investigated to compare their optical transmittances and surface roughness. Interestingly, the optical transmittance of PDMS from the 3D-printed mold was significantly increased via bonding two single PDMS layers. To evaluate the applicability of the replicated PDMS devices from the 3D-printed mold, we performed droplet generation in the PDMS microchannels, comparing the same device from a conventional Si-wafer mold. This study provides a fundamental understanding of prototyping microstructures from the DLP-based 3D-printed mold.



## INTRODUCTION

Microfluidics has achieved significant progress that demonstrates the promising potential for real-world applications. Due to its advantages, such as small sample volume, fast reaction time, and high throughput, microfluidics has been widely studied in various research fields, such as drug screening,<sup>1</sup> bioprinting,<sup>2</sup> organs-on-a-chip,<sup>3</sup> cell mechanics,<sup>4</sup> and point-of-care testing (POCT).<sup>5</sup> Despite the advance in microfluidics, conventional manufacturing technologies continue to rely heavily on polymer microfabrication techniques, including soft lithography,<sup>6</sup> hot embossing,<sup>7</sup> and injection molding,<sup>8</sup> which require long manufacturing time, high cost, and trained experts. As an alternative, additive manufacturing has gained popularity due to its versatility, flexibility, and low cost, making it an attractive option to overcome these limitations. In particular, three-dimensional (3D) printing, which utilizes a layer-by-layer manufacturing approach and digital tools to fabricate a complex design, has recently emerged as a promising solution.<sup>9–11</sup>

3D printing technology offers high throughput and parallel microstructure fabrication efficiency compared to the labor-intensive and time-consuming soft lithography process. For instance, the parallel fabrication of identical microstructure designs or various designs of multiple microstructure parameters can be achieved at once. Due to high efficiency and rapid prototyping capabilities of 3D printing technology, various 3D-printed microstructures have been directly

implemented in microfluidic studies.<sup>12–15</sup> Nevertheless, the surface properties, biocompatibility, and transparency of different resins have presented significant challenges in the practical use of 3D-printed structures in microfluidics.<sup>16–18</sup> For example, a rough surface profile in a 3D-printed microchannel can cause liquid dead volume or inconsistent surface treatment.<sup>19</sup> In addition, photoinitiators included in 3D printing resin or residual uncured resin monomers may exhibit toxicity to cells and adversely affect cellular behavior.<sup>20</sup> In order to overcome cytotoxicity, a poly(ethylene glycol) diacrylate (PEGDA)-based biocompatible resin was developed.<sup>21</sup> However, the developed resin showed poor cell adherence, and PEGDA may have a limited mechanical strength, which limits microfluidic applications that require high mechanical strength. Moreover, commercially available resins typically hinder optical detection due to their low transparency.<sup>22</sup> Additional polishing of the 3D-printed microstructure is required to modify its optical transparency.<sup>23,24</sup>

Received: April 28, 2023

Accepted: May 9, 2023

Published: May 18, 2023



Poly(dimethylsiloxane) (PDMS) microstructures, which are biocompatible and optically transparent, can be easily replicated from the 3D-printed mold as a promising way to accelerate microfluidic research.<sup>25–30</sup> The digital light projection (DLP) printing method is frequently employed for fabricating 3D structures layer by layer through a projected light source, such as ultraviolet (UV), to polymerize a photopolymer resin.<sup>31</sup>

This paper investigates the characteristics of PDMS obtained from a DLP-based 3D-printed mold and compares them with those obtained from a conventional silicon (Si) wafer mold. Characteristics of PDMS fabricated using 3D-printed molds under various printing conditions, such as arrangement method and slice thickness, were investigated to find the optimal settings for microfluidics. The transparency of single and double layers of PDMS from the different molds was examined, and scanning electron microscopy (SEM) images were taken to further investigate the surface roughness of PDMS obtained under various printing conditions. Fluorescence and colorimetric assays were also performed to ensure that the transparency of PDMS microchannels from the 3D-printed molds does not hinder signal reading. Finally, the conventional microchannels for generating microdroplets were fabricated from the Si wafer and the 3D-printed molds, and the size distribution of the generated droplets from different mold types was evaluated for feasibility.

## MATERIALS AND METHODS

**DLP 3D Printing.** A DLP 3D printer (Pro 4K65; Asiga, Alexandria, Australia) was used to fabricate the mold. The selected printer has a large build volume of 176 mm × 99 mm × 200 mm for *x*, *y*, and *z* axes. A PlasCLEAR resin (Asiga) was utilized for DLP-based 3D printing. The mold was designed with an Autodesk Inventor (Autodesk, San Francisco, CA). The STL files were modified using Composer software (Asiga) capable of controlling the printing parameters, such as arrangement method, light intensity, and slice thickness, for accurate printing results. The devised STL files were set with horizontal and vertical directions for an experiment. The slice thickness was set as either 25 or 50 μm for each printing direction. Depending on the printing directions and the slice thickness, the printing time of the structure was dramatically varied. After setting the optimal parameters, the desired 3D structure was printed and irradiated with UV light at 385 nm to cure the resin. The light intensity was set to 20 mW/cm<sup>2</sup> for enough exposure time to cure the resin. Finally, the microscales of features were successfully inscribed on the cured resin.

**Post-Treatment Process of a 3D-Printed Structure.** After printing, the remaining resin on the mold was removed according to the following: (1) the mold was rinsed with 100% ethanol and sonicated for 10 min in 100% isopropyl alcohol (IPA), (2) to ensure the resin removal, the mold was exposed to UV light for 3 min in a flash UV chamber (Asiga), (3) the UV-cured mold was autoclaved at 120 °C for 1 h, (4) the autoclaved mold was treated with oxygen plasma for 1 min, and (5) the plasma-treated mold was treated with trichloro-(1H,1H,2H,2H-perfluorooctyl) silane (Sigma-Aldrich, St. Louis, MO) in a vacuum chamber for 2 h for chemical vapor deposition. After the silane treatment, the mold is in a ready-to-use state.

**Micromachining of a Si Wafer.** The double-polished p-type wafer was used for the micromachining. Informal cleaning

was carried out prior to micromachining. The photoresistor, SU-8 2100 (K1 solution, Kwangmyung, Korea), was spin-coated on the wafer at 1500 rpm for 30 s (target thickness = 100 μm). As a prebaking step, the SU-8 coated wafer was incubated in a convection oven at 65 °C for 5 min and 90 °C for 20 min. An MA6 aligner (Karl-Süss, Garching, Germany) was then used to expose the UV light with 16 mW for 10 s. The wafer was incubated in the convection oven at 65 °C for 5 min and 90 °C for 12 min for the postbaking step. For the development, the microstructure-patterned wafer was immersed in an SU-8 developer for 10 min. The remaining developer was washed with IPA and deionized water and then bloomed with a nitrogen gun to remove any remaining liquids.

**PDMS Microchannel Fabrication.** PDMS was fabricated under identical conditions except for the thin PDMS membrane in all experiments. Generally, PDMS and the curing agent were mixed with a ratio of 10:1. The mixed PDMS was poured into each type of mold, Si wafer, and 3D-printed mold. For curing, the PDMS-poured mold was incubated in an oven at 85 °C for 30 min. The single PDMS layer (thickness = 2 mm) was finally fabricated by peeling off the mold. For the thin PDMS membrane fabrication, PDMS and the curing agent with a mixing ratio of 7:1 were prepared, and the PDMS mixture was spin-coated on the bare silicon wafer at 1500 rpm for 1 min and baked at 150 °C for 1 min. For PDMS–PDMS bonding, each layer was treated with oxygen plasma for 1 min, bringing the layers into contact. The bonded PDMS layers were incubated in an oven at 60 °C for 10 min to increase the bonding strength.

**Optical Analysis.** For investigation of the optical properties of the PDMS, a single PDMS layer was directly peeled off from the molds, and the double PDMS layers were used after bonding the single PDMS layer with the thin PDMS membrane. The light (wavelength = 515 nm) was emitted for the intuitive comparison, and the scattering tendency after PDMS penetration was observed. The distance between the PDMS layer and the background screen was set to be 12 cm. For quantitative analysis within the visible light range (from 350 to 800 nm), a ultraviolet/visible/near-infrared (UV/VIS/NIR) spectrophotometer (SolidSpec-3700; Shimadzu, Kyoto, Japan) was utilized to obtain the optical transmittance data for each wavelength with an interval of 5 nm.

**SEM Imaging.** The surface morphology of the PDMS replica and its mold was investigated with a scanning electron microscope (SU8230; Hitachi, Tokyo, Japan). The samples were mounted on the stub with double-sided adhesive tape. All of the samples were sputtered with platinum for 2 min prior to imaging. The SEM imaging was carried out at a 5 kV acceleration potential.

**Contact Angle Measurement.** The contact angle of the water droplet on the PDMS surface was measured with a contact angle analyzer (Phoenix-MT; SEO, Suwon, Korea). Three microliters of pure water was dropped onto the surface of PDMS from various conditions. For hydrophilic properties, the PDMS layer was treated with oxygen plasma treatment for 20 s, and the treated PDMS layer was immediately brought into the contact angle analyzer. The water drop image on the PDMS surface was taken using Surfaceware software (SEO), and the captured image was analyzed with ImageJ software (National Institute of Health, Bethesda, MD) for precise angle measurement. All images were taken at room temperature.

**FT-IR Measurements.** For chemical composition analysis, Fourier transform infrared (FT-IR) spectroscopy was carried

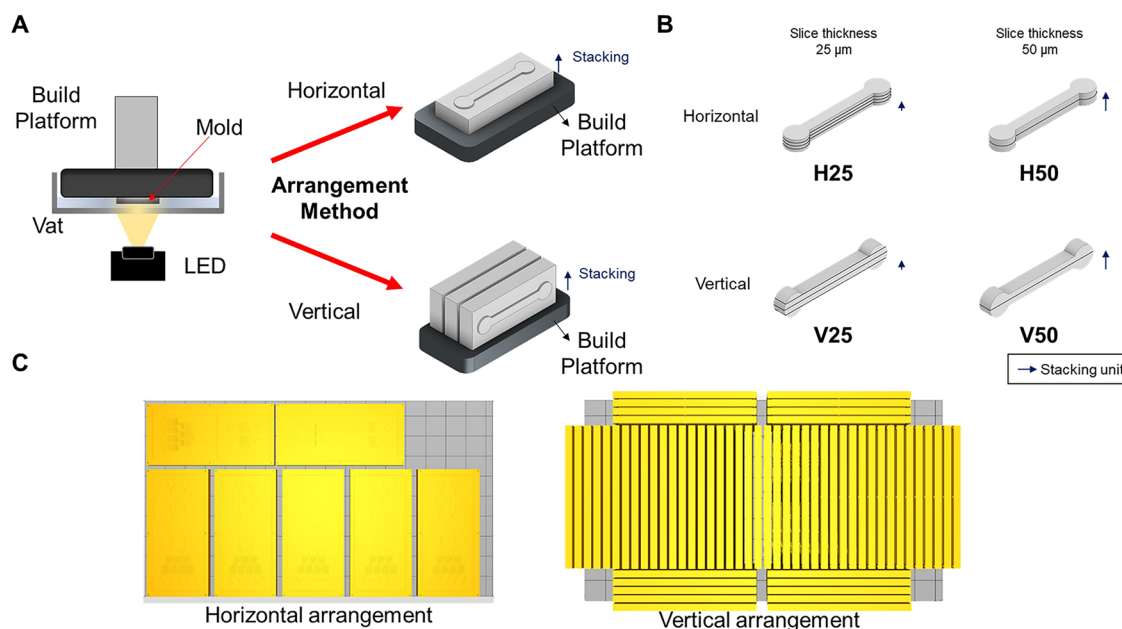


**Figure 1.** General concept of DLP printing based on different arrangement methods. (A) Schematic of the build platform and two types of arrangement methods: horizontal and vertical. (B) Schematic of layer addition based on different slice thicknesses. (C) Representative images for the comparison of productivity based on arrangement methods with an identical microfluidic device.

out via a Nicolet iS50 (Thermo Fisher Scientific Instrument, MA) in the range of 400–4000 nm. PDMS from each type of mold was tested individually, and the individual data were incorporated into a single graph for clear visualization.

**Characterization of Fluorescence and Colorimetric Assays.** The quantification of fluorescence and colorimetric assays was performed with the double-layer PDMS. Solutions of erioglaucine and fluorescein isothiocyanate (FITC) were obtained from Sigma-Aldrich and MK Science (Seoul, Korea), respectively, and used to characterize the colorimetric or fluorescence intensity in a microchannel. Each solution was diluted with distilled water for the preparation of 2×, 3×, and 4× diluted solutions. For the fluorescence reading, the image of the FITC-filled microchannel was taken by a charge-coupled device (CCD) camera (DP72; Olympus, Tokyo, Japan) attached to a fluorescence microscope (LX72; Olympus). For the colorimetric reading, the image of an erioglaucine-filled microchannel was taken by a stereomicroscope (SZX16; Olympus) equipped with the CCD camera. The images were further analyzed by ImageJ software. For colorimetric analysis, the percentage of blue pixels out of overall red, green, and blue (RGB) pixels was calculated according to the following equation:

$$\text{percentage of blue intensity} = \left( \frac{\text{blue pixels}}{\text{RGB pixels}} \right) \times 100(\%)$$

**Droplet Microfluidics.** The PDMS microchannel and the molds were fabricated under the same procedure as previously mentioned. To remove the effect of the plasma treatment after substrate bonding, the PDMS device was incubated overnight at 65 °C in an oven prior to the experiment. The inlets of the PDMS device were connected to two syringe pumps (KDS100; KD Scientific Inc., Holliston, MA) with the tubing. The droplet generation oil (1864005; Bio-Rad, Hercules, CA) and erioglaucine solution were injected into each inlet of the PDMS device at different flow rates of 0.7 and 0.3 mL/h,

respectively. The droplet generation and the cluster of droplets were captured by the stereomicroscope. The captured images were analyzed by ImageJ software to obtain the size distribution.

## RESULTS AND DISCUSSION

**System Setup and Arrangement Method.** The DLP printer mainly consists of a build platform on which a 3D-printed structure generates, a resin-containing vat, and a light source that emits light to harden the exposed resin (Figure 1A). Assuming the conventional rectangular shape of a microfluidic channel, the DLP printer can be used to generate a microchannel according to the arrangement, horizontally or vertically, as shown in Figure 1A. The horizontal condition is widely adopted in fabricating the desired structure due to rapid time consumption. In contrast, the vertical condition has not yet been investigated to determine whether it provides the optimal environment for DLP printing, albeit the long building time. The vertical condition maximizes the use of the z-axis, allowing more structures to be fabricated at once.

Figure 1B illustrates the slice thickness of DLP printing, indicating the height of each layer of the 3D-printed structure. The slice thickness is highly correlated to printing time, the targeted height, and resolution, requiring a careful selection for optimal printing conditions. In this work, two conditions for slice thickness were adopted: 25 and 50 μm. While the slice thickness being 25 μm generally demonstrates improved resolution, it sacrifices a long building time. On the other hand, the slice thickness of 50 μm shows a shorter building time but less resolution than that of 25 μm. In this work, the 3D printing results are abbreviated as follows: horizontal printing with a slice thickness of 25 μm as H25, horizontal printing with a slice thickness of 50 μm as H50, vertical printing with a slice thickness of 25 μm as V25, and vertical printing with a slice thickness of 50 μm as V50.

The productivity of each printing condition can be compared by arranging molds with the same design using

Composer software (Figure 1C). The horizontal arrangement can fabricate only seven molds, but the vertical direction can fabricate 60 molds at a time. The vertical arrangement can facilitate the use of space, consequently showing over eight times of output, which is outstanding for mass production. In addition, the software calculated the estimation time of fabrication, and productivity by printing condition can also be calculated (Table S1, Supporting Information). The vertical arrangement can facilitate mass production with rapid printing time per piece. To further validate that the identical 3D-printed structures are fabricated, 3D-printed structures were fabricated from the top-left corner, top-right corner, bottom-left corner, bottom-right corner, and center of the build platform and demonstrated that the structures did not vary (Figure S1, Supporting information).

**Optical Analysis of PDMS.** Optical transparency is one of the noticeable characteristics of PDMS obtained from different conditions of molds. Despite the same condition for PDMS curing, the optical transparency of PDMS layers from other types of molds varied significantly (Figure 2A). The apparent appearance of the PDMS layer from a micromachined Si wafer exhibited the highest transparency, but the PDMS layers from 3D-printed molds showed less transparency. The PDMS layers from H25 and H50 conditions were more opaque than those from the Si wafer. In addition, the PDMS layers from V25 and V50 conditions showed the greatest opaqueness. Such a phenomenon can be attributed to the surface roughness of the PDMS, which will be further discussed in the next section in detail. For the improvement in optical transparency, the thin PDMS membrane was permanently bonded to the single PDMS layer from different types of molds. While the PDMS from H25 and H50 conditions bonded smoothly to the PDMS membrane, the PDMS from the V25 condition showed some unbonded portions to the PDMS membrane on edge, and the V50 condition showed bonding failure. The PDMS membrane bonding increased the optical transparency, regardless of the printing conditions except for the V50 condition. While the PDMS from H25 and H50 conditions demonstrated an increase in optical transmittance at wavelengths higher than 400 nm, that at a low wavelength (<400 nm) showed low transmittance. However, the wavelength under 400 nm is the UV range while the visible spectrum range is from 400 to 700 nm, which is the range in which the optical transmittance was significantly increased. Therefore, there is almost no influence on the visible spectrum. The patterned regions on PDMS layers were still left opaque because this was attributed to the unbonded pattern with the capped air.

The fact that PDMS has different transparency depending on the type of mold can be attributed to light scattering. To verify such an assumption, the light (wavelength = 515 nm) in the visible spectrum was exposed to PDMS with/without the bonded thin PDMS membrane (Figure 2B). After penetration, the different light patterns were projected onto the background screen. The PDMS layer from the Si wafer did not show a significant variance in the light projection. However, the projection images of the PDMS layers from horizontally printed mold were similar to circular patterns and haze, but the PDMS layers from vertically printed mold showed a pattern that resembles a strip pattern and lattice. For further analysis, the light scattering after bonding the thin PDMS membrane was also investigated. Regardless of the mold types, the light scattering phenomenon was weakened after bonding the thin PDMS membrane, demonstrating improved optical trans-

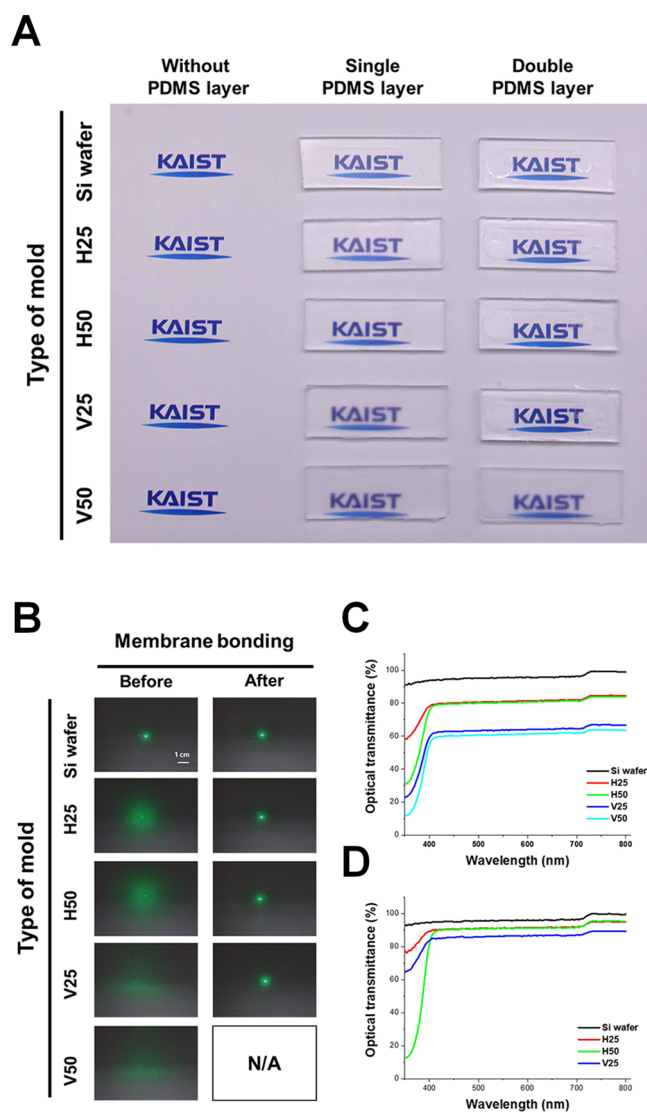


**Figure 2.** Optical analysis of PDMS layers from various types of molds. (A) Optical transparency and (B) laser scattering of PDMS layers from various molds before and after additional PDMS layer bonding. Optical transmittance of PDMS layers from various types of molds before (C) and after (D) bonding of the PDMS layer.

parency. As previously stated, since the PDMS layer from V50 failed to bind the membrane PDMS, the data were not acquired.

The quantitative optical transmittance was measured to delve into the phenomenon (Figure 2C). The measurement was carried out in the visible light range and its boundary (350–800 nm). The PDMS layer from the Si wafer exhibited approx. 95% of transmittance in visible light, while the transmittance of the PDMS layers from the 3D-printed molds decreased significantly. In particular, the PDMS layers from H25 and H50 conditions showed approx. 80% of transmittance, but the transmittance of the PDMS layers from the vertical condition was only approx. 60%. The transmittance measurement was also performed after the thin PDMS membrane bonding (Figure 2D). As previously mentioned, the PDMS layer from V50 was excluded due to the bonding failure. As expected, the optical transmittance of all of the samples from the 3D-printed molds was improved with the membrane bonding that supports the phenomenon explained

in Figure 2A,B. The PDMS layers from H25 and H50 conditions were adjacent to 90% of optical transmittance in visible light, similar to that of the PDMS layer from the Si wafer. In addition, the optical transmittance of the V25 condition nearly approached 80%, demonstrating improved optical transmittance. In this sense, the issue of optical transparency of PDMS layers from 3D-printed molds can be easily resolved by simply bonding other materials such as PDMS or glass slide.

**SEM Images of Molds and PDMS from Various Conditions.** Yabu et al. discovered that the optical transparency was attributed to the micro- and nanoscale geometry of the material surface.<sup>32</sup> The SEM images of the PDMS surface from different mold types were obtained to interpret the transparency issue. The surfaces of the SU-8 patterned Si wafer, the 3D-printed mold, and the PDMS replica from each type of mold were investigated. The simple microstructure of the PDMS replica and its mold were captured for comparison (Figure 3A). While the surface of the Si wafer exhibited the smoothest surface, the surface of 3D-printed molds was rougher. H25 and H50 conditions similarly showed the conspicuous microstructure with a rough surface. However, the V25 and V50 conditions demonstrated the microstructure with a stripe pattern. The resolution of the microstructure also showed a strong correlation to the slice thickness in a way that the gap between the two microstructures was not identical to the originally designed gap distance. Such a phenomenon may be attributed to UV light scattering for resin curing. The H50 condition requires a longer distance between the build platform and the vat than the H25 condition. Since the scattered light moved long distances, the fine structure was not identically constructed.

For further investigation, SEM images of the cross section of the PDMS replicas from the Si wafer, H25, and V25 molds were taken (Figure 3B). The cross-sectional and tilted images of the PDMS replica from the Si wafer showed a smooth surface, while those of the PDMS replicas from H25 and V25 conditions demonstrated a rough surface. Along with Figure 3A, the surface of the PDMS replica from the V25 condition maintains the stripe pattern, indicating high surface roughness. The cross-sectional SEM images of the PDMS membrane-bonded PDMS from the previously mentioned mold types were taken. As previously explained, the PDMS membrane bonding makes up for the uneven PDMS surface, improving optical transmittance. The result implies that when a material such as liquid can physically fill the rough surface, the optical transparency increases by reducing the degree of light scattering (Figure S2, Supporting Information).

**Physical and Chemical Characteristics of PDMS from Various Mold Types.** Since surface wettability plays a significant role in microfluidics,<sup>33</sup> the physical properties of PDMS layers obtained from the conventional wafer mold and the 3D-printed molds were characterized. Contact angles of PDMS layers under various conditions—Si wafer, H25, H50, V25, V50—were measured. As shown in Figure 4A, the hydrophobic nature of the PDMS surface remains constant, regardless of the various mold types. While the PDMS layer from the Si wafer showed approx.  $104.69 \pm 5.17^\circ$ , that from H25, H50, V25, and V50 demonstrated  $116.18 \pm 3.37$ ,  $115.64 \pm 1.27$ ,  $118.31 \pm 3.98$ , and  $132.14 \pm 2.42^\circ$ , respectively. The increased contact angle can be attributed to the Wenzel equation, which states that the surface roughness contributes to a more hydrophobic surface. As shown in Figure 3, the

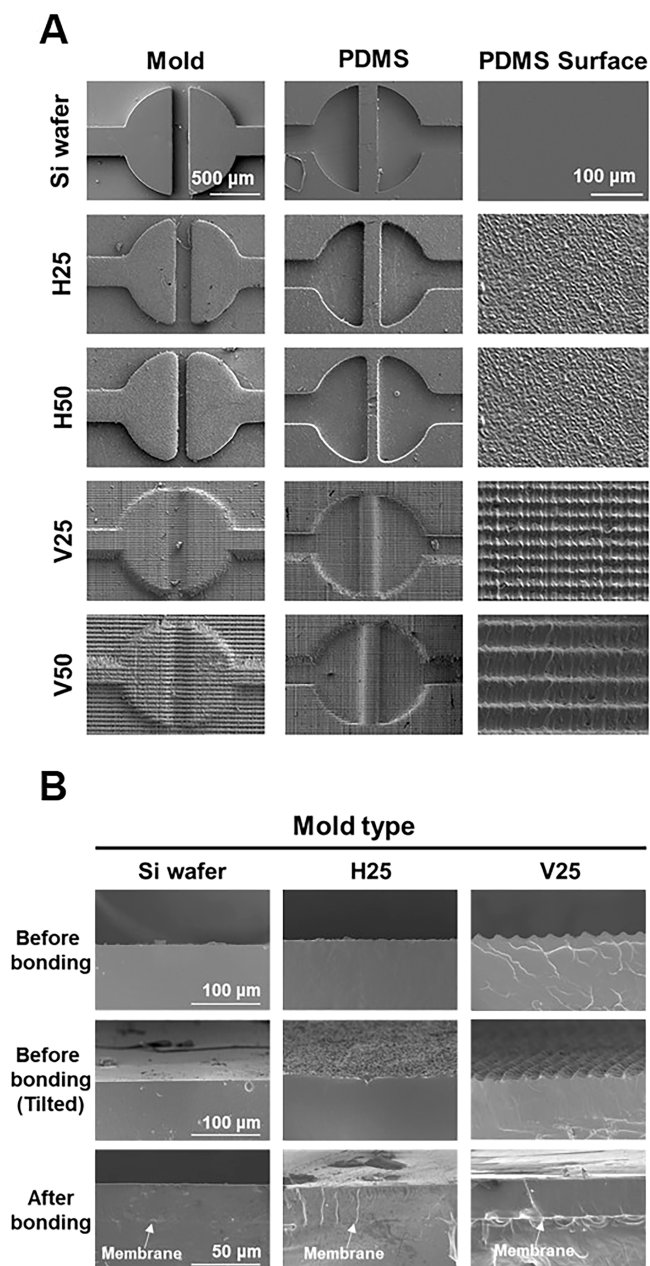


**Figure 3.** SEM images taken from various types of molds and their PDMS replicas. (A) SEM images of the same microstructure based on types of molds and their PDMS replicas. SEM images of the PDMS surface were further taken by magnification. (B) SEM images of the cross section of the PDMS replicas from different mold types.

surface roughness dramatically increased according to the printing conditions, resulting in a more hydrophobic PDMS surface, which was in line with the increased contact angles.

O<sub>2</sub> plasma treatment of PDMS is one of the most widely adopted techniques to temporarily change from the hydrophobic to hydrophilic properties of the PDMS surface. Contact angles after the plasma treatment were measured to investigate whether the hydrophilic property of the PDMS surface after treatment was observed, regardless of the mold types. Generally, irrespective of the mold types, the contact angle of the PDMS surface was significantly reduced, illustrating the hydrophilic property after the plasma treatment. However, the degree of hydrophilic property of the PDMS surface varied

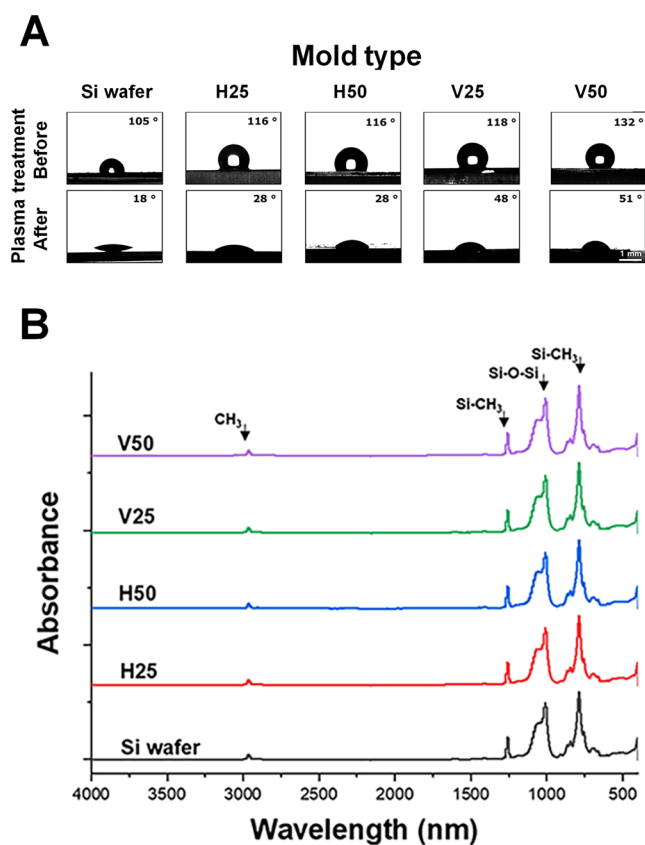


**Figure 4.** Contact angle and FT-IR measurement of PDMS layers from different mold types. (A) Contact angle of a water droplet and PDMS surface before and after O<sub>2</sub> plasma treatment ( $n = 3$ ). (B) FT-IR measurement of the PDMS surface for its chemical composition.

based on mold types. The contact angle of the PDMS surface from the wafer mold showed the most excellent hydrophilic property with approximately  $17.94 \pm 0.62^\circ$ . Regardless of slice thickness, the arrangement method highly influenced the degree of hydrophilic property. For H25 and H50 conditions, both the PDMS surface illustrated almost the same contact angles with  $27.85 \pm 3.36$  and  $27.84 \pm 1.11^\circ$ , respectively, to each other. The larger contact angle of the PDMS surface from H25 and H50 conditions than that from the wafer mold can be attributed to the Wenzel equation, which states that surface roughness influences the contact angle of solid and liquid.

Furthermore, the PDMS layers from V25 and V50 conditions demonstrated similar contact angles,  $48.43 \pm 1.79$  and  $50.57 \pm 4.68^\circ$ , respectively. Even after O<sub>2</sub> plasma treatment, such a larger contact angle further confirms the Wenzel equation that surface roughness highly affects the contact angle of solid and liquid, and the surface roughness of the vertical printing condition is higher than that of the horizontal printing condition. In fact, despite the plasma treatment, the relatively high contact angles of the PDMS layers from V25 and V50 explain the nonbonding phenomenon. The plasma treatment on a nonsmooth surface may reduce plasma efficiency, resulting in reduced bonding strength between PDMS and PDMS.

To verify the chemical properties, FT-IR data were obtained for all PDMS layers (Figure 4B). Based on the chemistry of PDMS, C–H stretching in CH<sub>3</sub> shows a peak at  $2962 \text{ cm}^{-1}$ . At  $1259 \text{ cm}^{-1}$ , CH<sub>3</sub> in Si–CH<sub>3</sub> is symmetrically bending, and Si–O–Si is stretching at  $1076$  and  $1018 \text{ cm}^{-1}$ . The last peak at the

wavenumber of  $798 \text{ cm}^{-1}$  exhibits the molecular vibration in Si–CH<sub>3</sub>, Si–C stretching, and CH rocking. All data from the different types of PDMS layers exhibit identical data, which means that all PDMS layers are chemically identical, regardless of mold type.

**Fluorescence and Colorimetric Assays.** Considering the difference in the optical transmittance of PDMS microchannels from various mold types, the feasibility of fluorescence and colorimetric assays in PDMS microchannels was tested. Various concentrations of FITC were injected into the microchannel, and the fluorescence signal in the PDMS microchannel was analyzed (Figure S3, Supporting Information). The average fluorescence signal in a microchannel showed similar signal intensity among the same FITC concentration, regardless of the mold type (Figure 5A). The general tendency of fluorescence signals in the PDMS microchannels from various mold types demonstrates a similarity to each other, as the decrease in the concentration of FITC results in a decreased fluorescence signal. Regardless of mold type, such comparable fluorescence signals of various

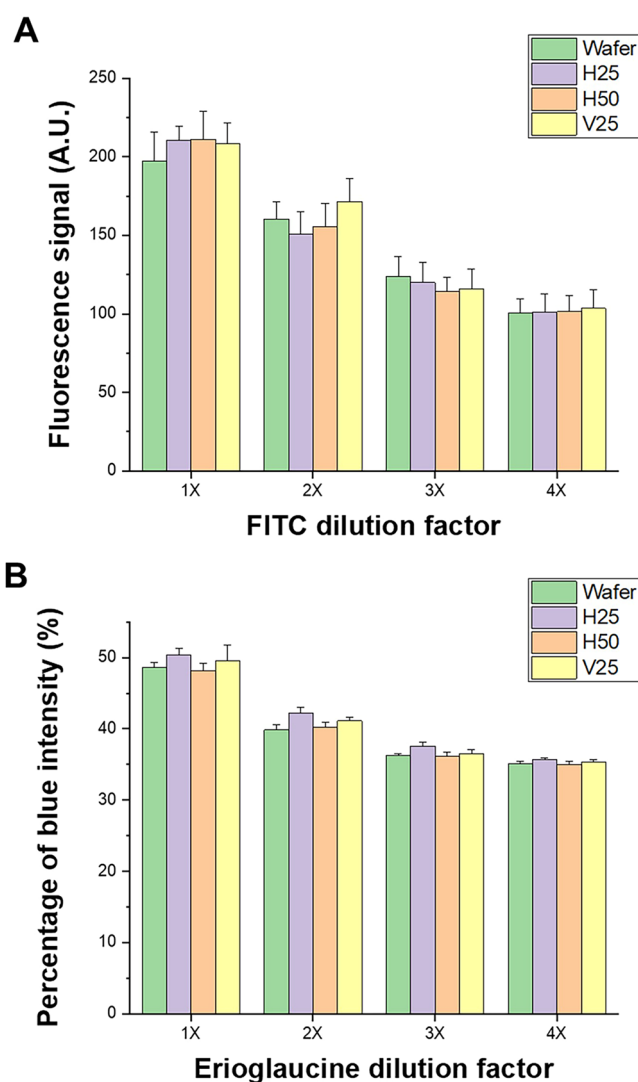


**Figure 5.** Fluorescence and colorimetric assays of PDMS microchannels from various mold types. (A) Fluorescence signal intensity with various FITC concentrations ( $n = 3$ ). (B) Percentage of blue intensity with various erioglaucine concentrations ( $n = 3$ ).

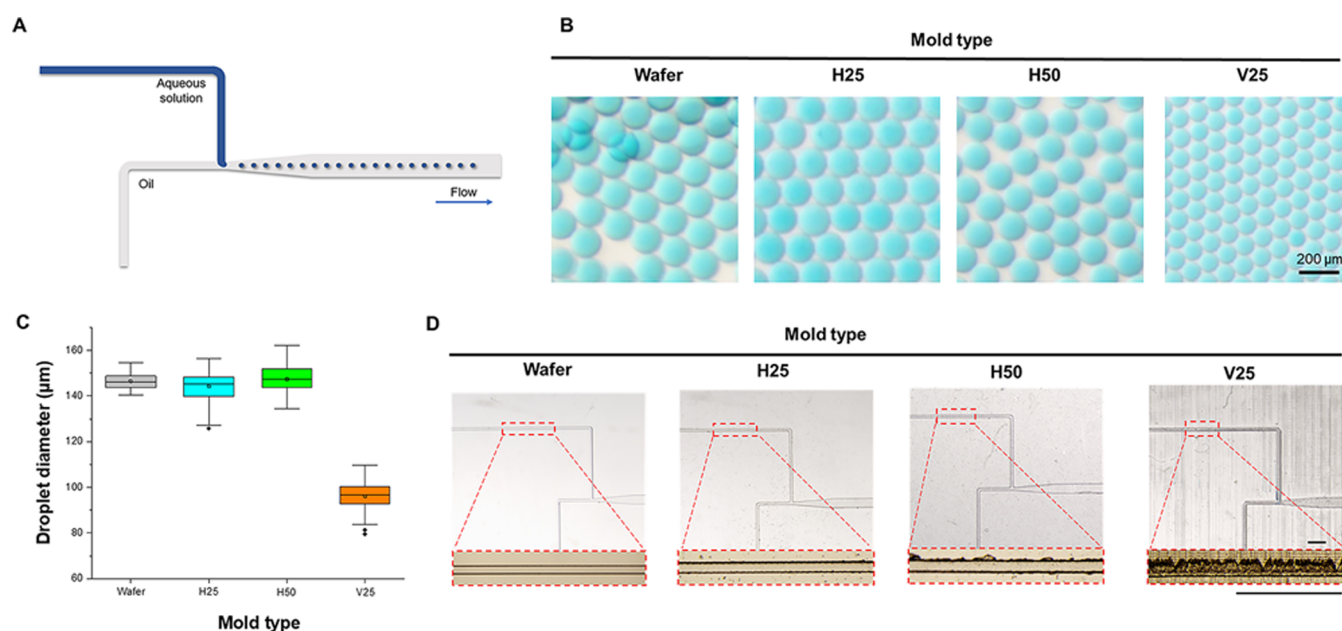


**Figure 6.** Droplet generation under various types of molds. (A) Schematic of droplet generation at a T-junction microchannel. (B) Representative pictures of generated droplets from various types of molds. (C) Size distribution of generated droplets under various conditions ( $n = 3$ ). (D) Representative images of PDMS microchannels for droplet generation from various mold types. The red square magnifies the generated PDMS-based microfluidic channel from various types of molds. Scale bar = 1 mm.

FITC concentrations demonstrate the suitable fluorescence signal reading.

The colorimetric signal was also analyzed to investigate the feasibility of the colorimetric assay (Figure S4, Supporting Information). The percentage of blue intensity out of the overall RGB intensity with various erioglaucine concentrations in the PDMS microchannels shows a comparable reading, regardless of the mold types (Figure 5B). The positive correlation between the concentration of erioglaucine solution and the percentage of blue pixels was observed in all types of molds. Therefore, fluorescence and colorimetric signal intensities in the mold types show no significant difference, confirming that the PDMS microchannels from the 3D-printed molds demonstrate a comparable performance with the Si wafer.

**Droplet Microfluidics.** Droplet generation is one of the promising applications of the microfluidic device, which is employed in various fields, such as droplet digital polymerase chain reaction (ddPCR),<sup>34</sup> drug discovery,<sup>35</sup> and cell sorting.<sup>36</sup> The conventional T-junction for droplet generation (Figure 6A) was designed to confirm the feasibility of microfluidic application in PDMS microchannels from various types of molds: Si wafer, H25, H50, and V25. Adjusting the flow rate is essential for successful droplet formation without jetting or droplet generation failure. The final flow rates were set to be 0.7 and 0.3 mL/h for the oil and aqueous phases, respectively, and the formation of droplets at the outlet was observed. Despite the rough surface profile of PDMS from the 3D-printed mold, the generated droplets, regardless of mold type, demonstrate a uniform size distribution with less than a coefficient of variation (CV) of 6% (Figure 6B). However, the droplets from V25 illustrate a relatively smaller average diameter than those from other mold types.

The diameters of the generated droplets from various mold types were numerically analyzed (Figure 6C). The average droplet size of all mold types demonstrates a similar result

except for V25. Considering that the droplet size of the PDMS microchannels of the Si wafer was 146.51  $\mu\text{m}$ , the average droplet diameters of H25 and H50, which are 144.22 and 147.45  $\mu\text{m}$ , respectively, show an insignificant difference. Such data indicate that the average diameter of droplets from the horizontal type mold deviates only 1% from that of the Si wafer, demonstrating a comparable performance.

While the horizontal type of mold illustrates remarkably comparable performance, the vertical type of mold shows a noticeable difference in average droplet size. The average droplet diameter from V25 was 96.21  $\mu\text{m}$ , which shows a difference of 34.33% from the Si wafer. To delve into a major reason for such a phenomenon, the geometries of the PDMS channel were investigated (Figure 6D). It was found that the microchannel on V25 was not correctly constructed. This phenomenon has been found in all V-type PDMS microchannels and only at the top side of the microchannels, regardless of their designs. A microscopic image of the 3D-printed mold was created for detailed analysis (Figure S5, Supporting Information). As a result, it was confirmed that the microchannel was not formed in the correct shape. This may be an innate trait of the V-series molds as the microchannel is stacked without the base, such as the build platform or previously stacked slice. This means that the microchannel is stacked on the empty space, so exposing the UV light precisely to the target location was difficult. After the base slice was stacked, the remaining slices were stably stacked in the desired slice thickness. Since the microchannel was stacked without the base, the misalignment of the stacked layers could have resulted in the uneven sidewall of the microchannel. In summary, the geometric difference of the microchannel on V25 affected the laminar flow in such a way that the droplet size distribution shifted significantly.

In addition, V25 showed the highest value for the CV at 6.0%. The Si wafer showed the smallest CV value, 2.1%, and H25 and H50 showed 4.3 and 4.0% similarity, respectively.

Surface roughness could disturb the laminar flow in the microchannel, which can lead to different results in microfluidic applications. For droplet generation, the size distribution and CV value of the horizontally printed molds varied within a small range. The H25 and H50 showed similar performance compared to the Si wafer, which can be tolerated for rapid prototyping of the microfluidic device. Incredibly, V25 showed a significantly different result than others, even with the same condition. Apart from the diameter issue, V25 was capable of droplet generation. This implies that V25 is inadequate for some applications requiring precise flow control; still, it is respectable with a simple demonstration.

## CONCLUSIONS

In this study, PDMS from a DLP-based 3D-printed mold with different printing conditions—arrangement method and slice thickness—was characterized and compared with that from a conventional Si wafer. The transparency of PDMS was reduced due to the rough surface of the 3D-printed mold, but the simple PDMS bonding dramatically increased the transparency. The physical and chemical properties of PDMS from various mold types were observed and demonstrated no significant difference with PDMS from the Si wafer apart from the surface roughness. Fluorescence and colorimetric assays confirmed that the reduced transparency did not interfere with the signal reading. The PDMS microchannel from the 3D-printed mold was finally applied to the conventional droplet generation to ensure microfluidic feasibility. While PDMS from H-series molds demonstrated comparable performance to that from the Si wafer, PDMS from V25 mold illustrated a significant difference due to high surface roughness and undesired microstructures. Nevertheless, the V-series mold is mass-producible and may be appropriate for the microfluidic application that is insensitive to flow conditions and employs either fluorescence or colorimetric assay. Hence, this study aids in using PDMS microchannels from DLP-based 3D-printed molds and provides criteria to consider when devising other PDMS microdevices from DLP-based 3D-printed molds.

## ASSOCIATED CONTENT

### Supporting Information

The Supporting Information is available free of charge at <https://pubs.acs.org/doi/10.1021/acsomega.3c02933>.

Productivity of the 3D printing condition with different arrangement methods and slice thickness (Table S1); microscopy images of the 3D-printed microchannel under various mold types and printing positions on the build platform (Figure S1); transparency of the PDMS microchannels (A) before filling with liquid, (B) after filling with water, and (C) after filling with erioglaucine solution (Figure S2); representative images of FITC-filled PDMS microchannels under various concentrations and mold types (Figure S3); representative images of erioglaucine solution-filled PDMS microchannels under various concentrations and mold types (Figure S4); and microscopy images of the V25 mold surface of the droplet generator (Figure S5) (PDF)

## AUTHOR INFORMATION

### Corresponding Author

Je-Kyun Park — Department of Bio and Brain Engineering, Korea Advanced Institute of Science and Technology

(KAIST), Daejeon 34141, Republic of Korea; [orcid.org/0000-0003-4522-2574](https://orcid.org/0000-0003-4522-2574); Phone: +82-42-350-4315; Email: [jekyun@kaist.ac.kr](mailto:jekyun@kaist.ac.kr)

## Authors

Dong Hyun Han — Department of Bio and Brain Engineering, Korea Advanced Institute of Science and Technology (KAIST), Daejeon 34141, Republic of Korea

Untaek Oh — Department of Bio and Brain Engineering, Korea Advanced Institute of Science and Technology (KAIST), Daejeon 34141, Republic of Korea

Complete contact information is available at:

<https://pubs.acs.org/10.1021/acsomega.3c02933>

## Author Contributions

<sup>‡</sup>D.H.H and U.O. contributed equally to this paper.

## Notes

The authors declare no competing financial interest.

## ACKNOWLEDGMENTS

This research was supported by the Challengeable Future Defense Technology Research and Development Program through the Agency for Defense Development (ADD) funded by the Defense Acquisition Program Administration (DAPA) in 2022 (No. UI220005TD).

## REFERENCES

- Schuster, B.; Junkin, M.; Kashaf, S. S.; Romero-Calvo, I.; Kirby, K.; Matthews, J.; Weber, C. R.; Rzhetsky, A.; White, K. P.; Tay, S. Automated microfluidic platform for dynamic and combinatorial drug screening of tumor organoids. *Nat. Commun.* **2020**, *11*, No. 5271.
- Colosi, C.; Shin, S. R.; Manoharan, V.; Massa, S.; Costantini, M.; Barbetta, A.; Dokmeci, M. R.; Dentini, M.; Khademhosseini, A. Microfluidic bioprinting of heterogeneous 3D tissue constructs using low-viscosity bioink. *Adv. Mater.* **2016**, *28*, 677–684.
- Huh, D.; Matthews, B. D.; Mammoto, A.; Montoya-Zavala, M.; Hsin, H. Y.; Ingber, D. E. Reconstituting organ-level lung functions on a chip. *Science* **2010**, *328*, 1662–1668.
- Armistead, F. J.; De Pablo, J. G.; Gadelha, H.; Peyman, S. A.; Evans, S. D. Cells under stress: an inertial-shear microfluidic determination of cell behavior. *Biophys. J.* **2019**, *116*, 1127–1135.
- Shin, S.; Kim, B.; Kim, Y. J.; Choi, S. Integrated microfluidic pneumatic circuit for point-of-care molecular diagnostics. *Biosens. Bioelectron.* **2019**, *133*, 169–176.
- Qin, D.; Xia, Y.; Whitesides, G. M. Soft lithography for micro- and nanoscale patterning. *Nat. Protoc.* **2010**, *5*, 491–502.
- Jeon, J. S.; Chung, S.; Kamm, R. D.; Charest, J. L. Hot embossing for fabrication of a microfluidic 3D cell culture platform. *Biomed. Microdevices* **2011**, *13*, 325–333.
- Ma, X.; Li, R.; Jin, Z.; Fan, Y.; Zhou, X.; Zhang, Y. Injection molding and characterization of PMMA-based microfluidic devices. *Microsyst. Technol.* **2020**, *26*, 1317–1324.
- Bhattacharjee, N.; Urrios, A.; Kang, S.; Folch, A. The upcoming 3D-printing revolution in microfluidics. *Lab Chip* **2016**, *16*, 1720–1742.
- Shin, S.; Hyun, J. Matrix-assisted three-dimensional printing of cellulose nanofibers for paper microfluidics. *ACS Appl. Mater. Interfaces* **2017**, *9*, 26438–26446.
- He, Y.; Wu, Y.; Fu, J.-Z.; Gao, Q.; Qiu, J.-J. Developments of 3D printing microfluidics and applications in chemistry and biology: a review. *Electroanalysis* **2016**, *28*, 1658–1678.
- Erkal, J. L.; Selimovic, A.; Gross, B. C.; Lockwood, S. Y.; Walton, E. L.; McNamara, S.; Martin, R. S.; Spence, D. M. 3D printed microfluidic devices with integrated versatile and reusable electrodes. *Lab Chip* **2014**, *14*, 2023–2032.

- (13) Bazaz, S. R.; Rouhi, O.; Raoufi, M. A.; Ejeian, F.; Asadnia, M.; Jin, D.; Warkiani, M. E. 3D printing of inertial microfluidic devices. *Sci. Rep.* **2020**, *10*, No. 5929.
- (14) Enders, A.; Siller, I. G.; Urmann, K.; Hoffmann, M. R.; Bahnemann, J. 3D printed microfluidic mixers—a comparative study on mixing unit performances. *Small* **2019**, *15*, No. 1804326.
- (15) Kamat, A. M.; Pei, Y.; Jayawardhana, B.; Kottapalli, A. G. P. Biomimetic soft polymer microstructures and piezoresistive graphene MEMS sensors using sacrificial metal 3D printing. *ACS Appl. Mater. Interfaces* **2021**, *13*, 1094–1104.
- (16) Chen, C.; Mehl, B. T.; Munshi, A. S.; Townsend, A. D.; Spence, D. M.; Martin, R. S. 3D-printed microfluidic devices: fabrication, advantages and limitations—a mini review. *Anal. Methods* **2016**, *8*, 6005–6012.
- (17) Quero, R. F.; da Silveira, G. D.; da Silva, J. A. F.; de Jesus, D. P. Understanding and improving FDM 3D printing to fabricate high-resolution and optically transparent microfluidic devices. *Lab Chip* **2021**, *21*, 3715–3729.
- (18) Moreno-Rivas, O.; Hernández-Velázquez, D.; Piazza, V.; Marquez, S. Rapid prototyping of microfluidic devices by SL 3D printing and their biocompatibility study for cell culturing. *Mater. Today: Proc.* **2019**, *13*, 436–445.
- (19) Gross, B. C.; Anderson, K. B.; Meisel, J. E.; McNitt, M. I.; Spence, D. M. Polymer coatings in 3D-printed fluidic device channels for improved cellular adherence prior to electrical lysis. *Anal. Chem.* **2015**, *87*, 6335–6341.
- (20) Mi, S.; Du, Z.; Xu, Y.; Sun, W. The crossing and integration between microfluidic technology and 3D printing for organ-on-chips. *J. Mater. Chem. B* **2018**, *6*, 6191–6206.
- (21) Warr, C.; Valdoz, J. C.; Bickham, B. P.; Knight, C. J.; Franks, N. A.; Chartrand, N.; Van Ry, P. M.; Christensen, K. A.; Nordin, G. P.; Cook, A. D. Biocompatible PEGDA resin for 3D printing. *ACS Appl. Bio. Mater.* **2020**, *3*, 2239–2244.
- (22) Mehta, V.; Rath, S. N. 3D printed microfluidic devices: a review focused on four fundamental manufacturing approaches and implications on the field of healthcare. *Bio-Des. Manuf.* **2021**, *4*, 311–343.
- (23) Knowlton, S.; Yu, C. H.; Ersoy, F.; Emadi, S.; Khademhosseini, A.; Tasoglu, S. 3D-printed microfluidic chips with patterned, cell-laden hydrogel constructs. *Biofabrication* **2016**, *8*, No. 025019.
- (24) Beckwith, A. L.; Borenstein, J. T.; Velasquez-Garcia, L. F. Monolithic, 3D-printed microfluidic platform for recapitulation of dynamic tumor microenvironments. *J. Microelectromech. Syst.* **2018**, *27*, 1009–1022.
- (25) Chan, H. N.; Chen, Y.; Shu, Y.; Chen, Y.; Tian, Q.; Wu, H. Direct, one-step molding of 3D-printed structures for convenient fabrication of truly 3D PDMS microfluidic chips. *Microfluid. Nanofluid.* **2015**, *19*, 9–18.
- (26) Hwang, Y.; Paydar, O. H.; Candler, R. N. 3D printed molds for non-planar PDMS microfluidic channels. *Sens. Actuators, A* **2015**, *226*, 137–142.
- (27) Villegas, M.; Cetinic, Z.; Shakeri, A.; Didar, T. F. Fabricating smooth PDMS microfluidic channels from low-resolution 3D printed molds using an omniphobic lubricant-infused coating. *Anal. Chim. Acta* **2018**, *1000*, 248–255.
- (28) Kamei, K.-i.; Mashimo, Y.; Koyama, Y.; Fockenber, C.; Nakashima, M.; Nakajima, M.; Li, J.; Chen, Y. 3D printing of soft lithography mold for rapid production of polydimethylsiloxane-based microfluidic devices for cell stimulation with concentration gradients. *Biomed. Microdevices* **2015**, *17*, No. 36.
- (29) Comina, G.; Suska, A.; Filippini, D. PDMS lab-on-a-chip fabrication using 3D printed templates. *Lab Chip* **2014**, *14*, 424–430.
- (30) Bazaz, S. R.; Kashaninejad, N.; Azadi, S.; Patel, K.; Asadnia, M.; Jin, D.; Warkiani, M. E. Rapid softlithography using 3D-printed molds. *Adv. Mater. Technol.* **2019**, *4*, No. 1900425.
- (31) Amini, A.; Guijt, R. M.; Themelis, T.; De Vos, J.; Eeltink, S. Recent developments in digital light processing 3D-printing techniques for microfluidic analytical devices. *J. Chromatogr. A* **2023**, *1692*, No. 463842.
- (32) Yabu, H.; Shimomura, M. Single-step fabrication of transparent superhydrophobic porous polymer films. *Chem. Mater.* **2005**, *17*, 5231–5234.
- (33) Yin, Q.; Guo, Q.; Wang, Z.; Chen, Y.; Duan, H.; Cheng, P. 3D-printed bioinspired Cassie–baxter wettability for controllable microdroplet manipulation. *ACS Appl. Mater. Interfaces* **2020**, *13*, 1979–1987.
- (34) Park, J.; Lee, K. G.; Han, D. H.; Lee, J. S.; Lee, S. J.; Park, J. K. Pushbutton-activated microfluidic dropper for droplet digital PCR. *Biosens. Bioelectron.* **2021**, *181*, No. 113159.
- (35) Shembekar, N.; Chaipan, C.; Utharala, R.; Merten, C. A. Droplet-based microfluidics in drug discovery, transcriptomics and high-throughput molecular genetics. *Lab Chip* **2016**, *16*, 1314–1331.
- (36) Mazutis, L.; Gilbert, J.; Ung, W. L.; Weitz, D. A.; Griffiths, A. D.; Heyman, J. A. Single-cell analysis and sorting using droplet-based microfluidics. *Nat. Protoc.* **2013**, *8*, 870–891.